Article

Resonant bonding, multiband thermoelectric transport and native defects in n-type BaBiTe3-xSex (x = 0, 0.05 and 0.1)

S. Maier, S. Ohno, G. Yu, S. D. Kang, T. C. Chasapis, V. A. Ha, S. A. Miller, D. Berthebaud, M. G. Kanatzidis, G.-M. Rignanese, G. Hautier, G. J. Snyder, and F. Gascoin

Chem. Mater., **Just Accepted Manuscript** • DOI: 10.1021/acs.chemmater.7b04123 • Publication Date (Web): 04 Dec 2017

Resonant bonding, multiband thermoelectric transport and native defects in n-type $BaBiTe_{3-x}Se_x$ (x = 0, 0.05 and 0.1)

S. Maier[1], S. Ohno[2,3], G. Yu[4], S. D. Kang[2,3], T. C. Chasapis[3], V. A. Ha[4], S. A. Miller[3], D. Berthebaud[1], M. G. Kanatzidis[5], G.-M. Rignanese[4], G. Hautier[4], G. J. Snyder[3] and F. Gascoin[1]*

[1]*Laboratoire CRISMAT UMR 6508 CNRS ENSICAEN, 6 boulevard du Maréchal Juin, 14050 Caen Cedex 04, France*

[2]*Department of Applied Physics and Materials Science, California Institute of Technology, CA 91125, USA*

[3]*Department of Materials Science and Engineering, Northwestern University, Evanston, IL 60208, USA*

[4]*Institute of Condensed Matter and Nanosciences (IMCN), Université catholique de Louvain, 1348 Louvain-la-Neuve, Belgium*

[5]*Chemistry Department, Northwestern University, Evanston, IL 60208, USA*

*Corresponding author. Tel: +33-2-31452605. Fax: +33-2-31951600.
E-mail address: franck.gascoin@ensicaen.fr (F. Gascoin).

Abstract

The unique crystal structure of $BaBiTe_3$ containing Te···Te resonant bonds and its narrow band gap motivated the systematic study of the thermoelectric transport properties of $BaBiTe_{3-x}Se_x$ (x = 0, 0.05 and 0.1) presented here. This study gives insight in the chemical bonding and thermoelectric transport properties of $BaBiTe_3$. The study shows that the presence of Te···Te resonant bonds in $BaBiTe_3$ is best described as a linear combination of interdigitating $(Te^{1-})_2$ side groups and infinite Te_n chains. Rietveld X-ray structure refinements and extrinsic defect calculations reveal that the substitution of Te by Se occurs preferentially on the Te4 and Te5 sites, which are not involved in Te···Te bonding. This work strongly suggests that both, multiband effects and native defects play an important role in the transport properties of $BaBiTe_{3-x}Se_x$ (x = 0, 0.05 and 0.1). The carrier concentration of $BaBiTe_3$ can be tuned via Se substitution ($BaBiTe_{3-x}Se_x$ with x = 0, 0.05 and 0.1) to values near those needed to optimize the thermoelectric performance. The thermal conductivity of $BaBiTe_{3-x}Se_x$ (x = 0, 0.05 and 0.1) is found to be remarkably low (ca. 0.4 $Wm^{-1}K^{-1}$ at 600 K), reaching values close to the glass limit of $BaBiSe_3$ (0.34 $Wm^{-1}K^{-1}$) and $BaBiTe_3$ (0.28 $Wm^{-1}K^{-1}$). Calculations of the defect formation energies in $BaBiTe_3$ suggest the presence of native Bi_{Ba}^{+1} and Te_{Bi}^{+1} antisite defects, which are low in energy and likely responsible for the native n-type conduction and the high carrier concentration (ca. 10^{20} cm^{-3}) found for all samples. The analyses of the electronic structure of $BaBiTe_3$ and of the optical absorption spectra of $BaBiTe_{3-x}Se_x$ (x = 0, 0.05, 0.1 and 3) strongly suggest the presence of multiple electron pockets in the conduction band (CB) in all samples. These analyses also provide a possible explanation for the two optical transitions observed for $BaBiTe_3$. High-temperature optical absorption measurements and thermoelectric transport analyses indicate that bands higher in the conduction band converge with the conduction band minimum (CBM) with increasing temperature and contribute to the thermoelectric transport

properties of $BaBiTe_3$ and $BaBiTe_{2.95}Se_{0.05}$. This multiband contribution can account for the ~50 % higher zT_{max} of $BaBiTe_3$ and $BaBiTe_{2.95}Se_{0.05}$ (~0.4 at 617 K) compared to $BaBiTe_{2.9}Se_{0.1}$ (~0.2 at 617 K), for which no such contribution was found. The increase in the band offset between the CBM and bands higher in the conduction band with respect to the selenium content is one possible explanation for the absence of multiband effects in the thermoelectric transport properties of $BaBiTe_{2.9}Se_{0.1.}$

Introduction

Polychalcogenides exhibit a strikingly diverse crystal chemistry due to the formation of homonuclear and often resonant or hypervalent bonds between negatively charged chalcogen atoms (Q). This highly diverse anion chemistry led to the discovery of a vast number of new compounds with interesting physical properties over the past decades.[1-6] Within the family of polychalcogenides there are several examples with promising thermoelectric properties such as $HfTe_5$[7], $Ba_3Cu_{14-\delta}Te_{12}$[8] and $BaCu_{5.7}Se_{0.6}Te_{6.4}$[9] and $A_2BaCu_8Te_{10}$ (A = K, Rb, Cs).[10] Many of them possess low thermal conductivities, which can be well explained by their complex crystal structures, while their overall electronic transport properties are often poorly understood. Since it was realized that multi-valley bands[11,12] and band convergence[13,14] of multiple valence or conduction bands can result in high thermoelectric efficiencies, it is of interest to look deeper into the thermoelectric transport properties of polychalcogenides with complex crystal structures since many of them possess complex electronic structures and inherently low thermal conductivities.

The polytelluride compound $BaBiTe_3$, isostructural to $BaBiSe_3$[15] and $BaSbTe_3$[15], was first discovered by Chung et al.[16] and its thermoelectric transport properties were measured on single crystals. The unique part of the crystal structure of $BaBiTe_3$ is the parallel stripes of weak Te···Te bonding, the nature of which is still not entirely understood. $BaBiTe_3$ is an ideal candidate for fulfilling the requirements of a phonon glass and an electron crystal, which according to Slack results in both a low thermal and a high electrical conductivity needed for thermoelectrics.[17] The rigid, one-dimensional $[Bi_4Te_{10}]_\infty$ rods in the structure allow facile electronic conduction, while the heavy Ba atoms and weak Te···Te bonding result in a low thermal conductivity similar to previously studied compounds containing Ba or Tl.[18-23] In addition, the electrostatic repulsion between the lone pairs of Bi and the neighboring Te atoms can lead to strong anharmonicities in the lattice vibrations and hence low phononic thermal conductivities (κ_{ph}) close to the amorphous limit.[24-27] Low-temperature thermoelectric measurements of both p- and n-type single crystalline $BaBiTe_3$[16], electronic band structure calculations[28] gave a first impression of its promising thermoelectric properties. A pressure dependent study of the thermoelectric properties of p-type $BaBiTe_3$ single crystals[29] and a recent study of K and La substituted variants of $BaBiTe_3$[30] showed it was of further interest.

Here we study the Te···Te bonding in $BaBiTe_3$ and the origin of the two, previously observed[16] optical transitions in order to understand the electronic and thermoelectric transport properties and the intrinsic defect chemistry of $BaBiTe_3$. Understanding the chemical bonding is crucial since the type of bonding (metallic, covalent, ionic) can significantly affect the physical properties by controlling the degree of electron delocalization. The main objectives for alloying $BaBiTe_3$ with Se were to reduce its thermal conductivity, determine the minimum thermal conductivity, and to optimize its carrier concentration.

Experimental and computational details

Synthesis

An amount of 10 g of fine polycrystalline powders of $BaBiTe_{3-x}Se_x$ (x = 0, 0.05, 0.1 and 3) were obtained by ball milling (700 rpm, 15 milling cycles with a milling time of 2 min per cycle) starting from a stoichiometric mixture of Ba pieces (Alfa Aesar, 99+%), Bi powder (Alfa Aesar, 99.99 %) Se powder (Alfa Aesar, 99.999%) and Te powder (Alfa Aesar, 99.999+ %). All elements were stored under inert atmosphere and Se shots and Te lumps were freshly powdered before each reaction. A planetary micro mill Pulverisette7 (Fritsch, Germany), tungsten carbide reaction containers (20 ml) and seven 10 mm tungsten carbide balls were used for all syntheses.

Spark plasma sintering and shaping

An amount of 5 g of ball milled powder was densified by spark plasma sintering (HP D 25/1, FCT, Germany) using high density graphite dies (Carbon-Lorraine, France) resulting in cylindrical samples with a diameter and thickness of 15 mm and 5 mm respectively. A mechanical pressure of 45 MPa was applied and the densification was conducted for 30 min at 500 °C with a heating rate of 23 $°Cmin^{-1}$ up to 250 °C and 6 $°Cmin^{-1}$ between 250 °C and 500 °C and a cooling rate of 16 $°Cmin^{-1}$. During cooling the pressure was decreased to 32 MPa. Densities of 6.44 g/cm^3(96 % of ρ_{calc}), 6.14 g/cm^3(91% of ρ_{calc}), 5.6 g/cm^3 (84% of ρ_{calc}) and 6.37 g/cm^3 (99.5 % of ρ_{calc}) were obtained for x = 0, 0.05, 0.1 and 3, respectively. Disc shaped samples were obtained by cutting slices of 1 mm thickness perpendicular to the pressing direction.

Powder X-ray diffraction (PXRD) and Rietveld refinements

PXRD patterns were recorded before and after spark plasma sintering in order to confirm the average crystal structure. PXRD data of all samples was collected in 2h within a 2θ range of 5°-120° using a X'Pert Pro MPD diffractometer (PANalytical, Netherlands) and Cu-K$\alpha_{1/2}$ radiation ($\lambda_{1/2}$ = 1.54060/1.54439 Å). Rietveld refinements on PXRD patterns after spark plasma sintering were performed using the software FULLPROF.[31] The pseudo-Voigt function $pV(x) = \eta L(x) + (1-\eta)G(x)$ was used to model the peak shape with L(x) and G(x) representing the corresponding Lorentzian and Gaussian contributions. Further refined parameters are the FWHM parameters, the scale factor, zero shift, lattice parameters, isotropic displacement parameters, the preferred orientation parameter Pref1, background parameters and the site occupancy factors (s.o.f.). The modified March's function was used to treat preferred orientation.

Thermoelectric characterization

The thermal conductivities were calculated from the experimental densities, heat capacity (c_p), and the measured thermal diffusivities (D_{th}) using a LFA457 MicroFlash (Netzsch, Germany) laser flash system. The heat capacity was assumed to be $C_p = 3k_b$/atom according to the Dulong-Petit approximation. All measured thermal diffusivities are provided as supplementary information.

Electrical resistivity (ρ), hall carrier concentration (n) and mobility (μ) were measured on an in-house built measurement system[32] using the van der Pauw method and pressure-assisted Mo contacts. A magnetic field of 2T was applied during the hall measurements. The Seebeck coefficient was measured using a home-built measurement system[33] and Chromel-Nb thermocouples.

Scanning electron microscopy (SEM) and energy dispersive X-ray spectroscopy (EDS)

To analyze microstructure and chemical composition (by energy dispersive X-ray spectroscopy, EDS), a scanning electron microscope (Hitachi S-3400N-II: Variable-pressure tungsten filament SEM equipped with Oxford INCAx-act SDD EDS system) was used. The analyses were performed on polished surfaces after having measured the thermoelectric properties.

Optical absorption measurements

Mid-Infrared (~ 0.08 – 0.7 eV) diffuse reflectance (R) spectra of $BaBiTe_{3-x}Se_x$ (x = 0, 0.05 and 0.1) were collected under Argon atmosphere in the temperature range 300 – 500 K with a Nicolet 6700 FTIR Spectrometer equipped with a Praying Mantis attachment and a high-temperature stage from Harric Scientific Instruments. A KBr standard was used as reference. The room temperature diffuse reflectance of $BaBiSe_3$ was recorded with a Shimadzu UV-3101 PC double-beam, double-monochromator spectrophotometer operating from 200 nm to 2500 nm using $BaSO_4$ as a non-absorbing reflectance reference. The absorption spectra (α/s) were obtained using the Kubelka-Munk function, which gives a relationship between R and the absorption coefficient (α) and scattering coefficient (s) through

$$\left(\frac{\alpha}{s}\right) = \frac{(1-R)^2}{2R} \quad (1)$$

Speed of sound measurements and evaluation of Cahill's glass limit of the thermal conductivity (κ_{glass}) and the Debye temperature (θ_D) of $BaBiTe_3$ and $BaBiSe_3$

The longitudinal and transversal components of the speed of sound (v_L and v_T) were measured applying the pulse-echo method. A piezoelectric transducer coupled to the sample first sends the initial pulse, and then acts as a receiver measuring the echoed reflections (for details see supplementary information).[34] The speed of sound (v_s) was calculated from the longitudinal and transversal components v_L and v_T as follows:

$$v_s = \left[\frac{1}{3}\left(\frac{2}{v_T^3} + \frac{1}{v_L^3}\right)\right]^{-1/3} \quad (2)$$

From the speed of sound the Debye temperature (θ_D) and Cahill's glass limit of the thermal conductivity[35] (κ_{glass}) were calculated as follows:

$$\kappa_{\text{glass}} = \frac{1}{2}\left(\frac{\pi}{6}\right)^{\frac{1}{3}} k_B V^{-\frac{2}{3}}(2v_T + v_L) \quad (3)$$

$$\theta_D = \frac{\hbar\omega_D}{k_B} \quad (4)$$

where ω_D is the Debye frequency:

$$\omega_D = v_s \left(\frac{6\pi^2}{V}\right)^{1/3} \quad (5)$$

and where V corresponds to the unit cell volume per atom. The corresponding values of v_s, v_T, v_L, θ_D and ω_D can be found in the supplementary information.

Electronic structure, defect and COHP calculations

All density functional theory computations were performed using the Vienna ab initio software package (VASP)[36-39], PAW pseudopotentials[40], the generalized gradient approximation as implemented by Perdew, Burke and Ernzerhoff (PBE)[41] and a kinetic energy cutoff of 520 eV. A scissor (operator) shift was applied to the DFT band structure to correct the band gap and facilitate the comparison with experimental results. This correction is based on the empirical band gap obtained from optical absorption measurements (0.26 eV) and is consistent with the Goldsmid-Sharp band gap ($E_g = 2eS_{max}T_{max}$) of ca. 0.23 eV. For bulk calculations, the Brillouin zone was sampled by a 6×2×2 k-point mesh, while for the defect calculations a k-point mesh of 2×2×2 and a 3×1×1 supercell were used. A force convergence criterion of 0.005 eV/Å was adopted for all structural relaxations. The Crystal Orbital Hamilton population (COHP) curves were calculated using the LOBSTER[42] software. The defect formation energy D in a charge state q was calculated according to[43]

$$E_f[D^q] = E[D^q] + E_{corr}[D^q] - E[bulk] - \sum_i n_i\mu_i + q(\varepsilon_{VBM} + \Delta v) + \Delta\,\varepsilon_F \qquad (6)$$

$E[D^q]$ and $E[bulk]$ represent the total energy of the supercell with defects D in the charge state q and without any defects, respectively. n_i is the number of removed (n_i<0) or added (n_i>0) i-type atoms, and μ_i is the chemical potential. ε_{VBM} is the energy of the valence band maximum (VBM), and $\Delta\varepsilon_F$ is the Fermi energy (chemical potential) of the electrons relative to ε_{VBM}. $E_{corr}[D^q]$ and Δv are correction terms for the spurious image-image interaction and potential alignment.[44]

The chemical potential of the elements was obtained from a stable region of the Ba-Bi-Te phase diagram supported by all corresponding compounds present in the Materials Project database[45] using the pymatgen package.[46] The localized defect states with the charge q were corrected using the extended Freysoldt (Kumagai) scheme[47,48], while for delocalized defects, only a potential alignment between the bulk and neutral state was included. No band gap corrections have been applied on the defect computations.

Calculations of the optical absorption coefficient

The optical absorption coefficient (α) of $BaBiTe_3$ was calculated as a function of energy using the DFT (PBE) method and the random phase approximation approach (RPA). We neglect excitonic effects which we expect to be small in this material. A scissor (operator) shift was applied to the DFT band structure to correct the band gap and setting it consistently to the experimental value. A very dense k-point mesh of 34x9x9 corresponding to 450 k-points in the irreducible Brillouin zone is utilized to compute α. It is worth noting that only direct (i.e. no change in k-space) transitions are considered. Details concerning this type of calculations can be found in the supporting information of Ref. 49.

Results and Discussion

$BaBiTe_3$: Crystal structure and Te···Te bonding

The crystal structure of $BaBiTe_3$ (*cf.* Fig. 1) was first determined by Chung et al.[16] and the authors discussed two alternative Te···Te bonding situations, which can both describe the chemical bonding in the crystal structure.

Fig. 1 Crystal structure of $BaBiTe_3$ (black: Ba, light grey: Bi, dark grey: Te)

Their discussion is based on the Te···Te contacts (Te2-Te6: 3.098(2) Å and Te2···Te2: 3.170(2) Å) found between the rod-shaped columnar $[Bi_4Te_{10}]_\infty$ segments, which are built up by edge-sharing $BiTe_6$ octahedra. These Te···Te distances are larger compared to those found for normal covalent Te···Te single bonds (2.69-2.80 Å)[50], but well below typical Van der Waals interactions (4.0 Å - 4.2 Å)[51] so that Te2-Te2 and Te2-Te6 bonding interactions have to be taken into account. The first description rationalizes the structure as columnar $[Bi_4Te_{10}]_\infty$ segments alternating with infinite Te_n chains with Te···Te bonds only between the Te2 atoms, i.e. the Te_n chains are separated from the $[Bi_4Te_{10}]_\infty$ segments (*cf.* Fig. 2a).

Fig. 2 Previously described Te···Te bonding situations: a) Te_n chains and b) interdigitating $(Te^{1-})_2$ side groups; c) electron localization function of Te2 and Te6 (left) and -pCOHP curves of the Te2-Te2 and Te2-Te6 pairs (right) showing bonding interactions between Te2-Te2 and Te2-Te6; d) Te···Te resonant bonding, which can be understood as a linear combination between a) and b) and which involves three-center-four-electron (3*c*-4*e*) bonds; the bonding situation in d) is based on results from –pCOHP and ELF calculations shown in c); this new Te···Te bonding situation represents an electron delocalization over the Te2 and Te6 atoms, which reduces electrostatic repulsion between the Te2 and the Te6 atoms by minimizing their negative charge.

The second description rationalizes the structure as $[Bi_4Te_{10}(Te_2)]_n^{8n-}$ "herring-bone" shaped segments with interdigitating $(Te^{-1})_2$ side groups (*cf.* Fig. 2b). According to this description there are no bonds between the Te2 atoms and hence no infinite Te_n chains in the structure. Chung et al. found negative overlap populations from their extended Hückel calculations and concluded, based on these findings, that the crystal structure is better described as $[Bi_4Te_{10}(Te_2)]_n^{8n-}$ rods with $(Te^{1-})_2$ side groups and that there are no Te_n chains in the $BaBiTe_3$ crystal structure.

Our bonding analysis (*cf.* Fig. 2c) focuses on the bonding between Te2 and Te6. It is based on the evaluation of the Electron Localization Function (ELF) and the Crystal Orbital Hamilton Population (COHP) from density functional theory (DFT) in the generalized gradient approximation (GGA) computations. It unambiguously shows Te2-Te2 and Te2-Te6 bonding interactions consistent with the similar interatomic Te2-Te2 and Te2-Te6 distances. This new bonding situation is shown in Fig. 2d and can be rationalized as a linear combination of the two previous descriptions of the crystal structure given by Chung et al. in 1997 and it can be understood as a delocalization of electrons over the Te2 and Te6 atoms through the formation of three-center-four-electron (3*c*-4*e*) bonds. Such kind of resonant bonding can also explain the slightly longer bond lengths compared to classical Te···Te single bonds. The amount of occupied antibonding Te···Te p-states is slightly larger for the Te2···Te6 interactions compared to those between the Te2 atoms. Hence, the former are slightly weaker and the part of the $BaBiTe_3$ crystal structure that is dominated by Te···Te bonding is significantly strained due to the population of antibonding Te p-states.

Preferential site substitution of Se on the Te4 and Te5 sites

The crystal structure of $BaBiTe_{3-x}Se_x$ (x = 0, 0.05 and 0.1) was confirmed by PXRD and subsequent Rietveld refinements (*cf.* Fig. 3) based on the structural model obtained from a previous single crystal structure analysis of $BaBiTe_3$.[16]

Fig. 3 Rietveld refinements of experimental diffraction patterns (black) of a) $BaBiTe_3$, b) $BaBiTe_{2.95}Se_{0.05}$ and c) $BaBiTe_{2.9}Se_{0.1}$ recorded after spark plasma sintering. Calculated diffraction patterns, difference plots and reflection positions are depicted in red, blue and green, respectively; all experimental diffraction patterns were recorded after spark plasma sintering.

The site occupancy factors (s.o.f.) were refined for the Se substituted variants and we find that for x = 0.05 Se substitutes Te on the Te5 site (s.o.f. on Te5: 0.96/0.04 Te/Se), while Se substitutes Te on the Te4 and Te5 sites for x = 0.1 with a slight preference towards Te5 (s.o.f. on Te4: 0.9/0.1 Te/Se and s.o.f. on Te5: 0.78/0.22 Te/Se) and all other sites are fully occupied by Te. The corresponding results of the refinements are summarized in Table1 and the refined site occupancy factors are visualized exemplary for x = 0.1 in Fig. 4.

Table 1

Rietveld X-ray refinement results for $BaBiTe_{3-x}Se_x$ (x = 0, 0.05, 0.1).

Nominal composition	**$BaBiTe_3$**	**$BaBiTe_{2.95}Se_{0.05}$**	**$BaBiTe_{2.9}Se_{0.1}$**
Space group	$P2_12_12_1$ (No. 19)	$P2_12_12_1$ (No. 19)	$P2_12_12_1$ (No. 19)
Z	8	8	8
a (Å)	4.6147(1)	4.6103(1)	4.6056(1)
b (Å)	17.0365(4)	17.0287(4)	17.0171(5)
c (Å)	18.2990(4)	18.2785(4)	18.2503(5)
V (Å^3)	1439	1435	1430
ρ_{calc} (gcm^{-3})	6.733	6.746	6.702
Radiation	Cu-K$\alpha_{1/2}$, $\lambda_{1/2}$ = 1.54060/1.54439 Å		
2θ limits (°)	5.01-119.99	5.01-119.99	5.01-119.99
R_f	0.041	0.030	0.0401
R_{bragg}	0.048	0.036	0.0464
χ^2	1.48	1.62	1.64

Fig. 4 Parts of the $BaBiTe_{2.9}Se_{0.1}$ crystal structure with refined site occupancy factors (black: Se; grey: Te) illustrating the preferential site substitution of Te4 and Te5 by Se.

The clear changes in the lattice parameters (*cf.* Table 1) provide proof for a successful substitution of Te by Se, which can be confirmed by complementary EDS analyses. The elemental compositions extracted from EDS analyses are provided in Table 2 and the corresponding EDS spectra can be found in the supplementary information.

Table 2

Experimental compositions obtained from EDS analyses after thermoelectric characterization.

nominal composition	Ba (at. %)	Bi (at. %)	Te (at. %)	Se (at. %)	exp. composition
$BaBiTe_3$	20.18	20.86	58.96	-	$Ba_{1.03}Bi_{1.06}Te_3$
$BaBiTe_{2.95}Se_{0.05}$	19.99	21.03	58.12	0.86	$Ba_{1.01}Bi_{1.06}Te_{2.95}Se_{0.04}$
$BaBiTe_{2..90}Se_{0.10}$	19.86	21.11	57.16	1.87	$Ba_{1.01}Bi_{1.07}Te_{2.90}Se_{0.09}$

Since there is a preferential site substitution on the Te sites that are not involved in Te···Te bonding it can be concluded that a Se substitution of Te2 and/or Te6 atoms would destabilize the crystal structure and is therefore energetically not favorable. This is in good agreement with the extrinsic defect calculations (*cf.* supplementary information), which are further discussed in the section *Defect chemistry of BaBiTe3 and its Se substituted variants*.

Multiple electron pockets in the conduction band of $BaBiTe_3$ and orbital character of the conduction and valence band edges

The electronic structure of $BaBiTe_3$ was calculated and described previously.[16,28] Both studies could not entirely clarify the nature of the two transitions at ~ 0.28 eV (transition 1) and ~0.42 eV (transition 2) observed by diffuse reflectance (DR) measurements. This inspired us to recalculate the electronic structure in order to better understand the thermoelectric transport properties of $BaBiTe_3$ and the unusual shape of its experimental optical absorption spectrum, which is discussed in the section *Band convergence and an explanation for the two optical transitions*. It is important to note that spin-orbit coupling (SOC) does not significantly affect the overall band structure of $BaBiTe_3$ (*cf.* Fig. S3 in the supplementary information).[28]

It does, however significantly decrease the band gap. For narrow band gap materials it is difficult to obtain accurate band gaps from DFT-PBE calculations, which is why a scissor (operator) shift was applied to correct the band gap to the empirical value of 0.26 eV based on the optical band gap (experimental). This value is also consistent with calculations including SOC (*cf.* Fig. S3 in the supplementary information) and the Goldsmid-Sharp band gap (ca. 0.23 eV), which is discussed in the section *Thermoelectric transport properties of $BaBiTe_{3-x}Se_x$ (x = 0, 0.05, 0.1)*.

Fig. 5 a) Electronic structure of $BaBiTe_3$ with three electron pockets (CB_1, CB_2 and CB_3) and the atomic contributions to the conduction band minimum (CBM) and valence band maximum (the Fermi level is set to 0 eV); b) and c) correspond to the charge density distribution of the CBM and the valence band maximum (VBM) showing the strongest atomic contributions to the CBM and VBM; all calculations were performed using DFT-PBE.

Our results (*cf.* Fig. 5a) show three electron pockets (CB_1, CB_2 and CB_3) that lie close in energy in a range of only 100 meV and which are also present in Se substituted variants of $BaBiTe_3$ (*cf.* supplementary information). CB_1 and CB_3 are located along the **ΓZ** and **ΓX** directions, allowing nearly direct transitions from the VBM, while CB_2 is located along the **SY** direction allowing indirect transitions from the VBM.

The three electron pockets signify a material system with multiple valleys, which is an important feature since complex band structures with multi-valley bands (i.e. a large valley degeneracy N_v) and contributions of multiple conduction and/or valence bands can lead to high-efficiency thermoelectric materials as it was demonstrated for SnSe[52], $CoSb_3$[53] and $PbTe_{1-x}Se_x$.[13]

Knowing the atomic and orbital contributions to the band edges is important in order to understand which part of the crystal structure governs the electronic transport. This is especially true in compounds where ionic and covalent bonding coexists and where it is often assumed that the covalent part of the structure dominates the electronic transport. The band edges in $BaBiTe_3$ are dominated by Bi and Te states (*cf.* Fig. 5a). The strongest contribution to the valence band edge comes from the Bi*6p*-Te*5p* and Te*5p*-Te*5p* bonding states, while their corresponding antibonding states are the main contributors to the conduction band edge (*cf.* Fig.6). These Bi*6p*-Te*5p* and Te*5p*-Te*5p* contributions are also visualized in Fig. 5 (other contributions are not shown for clarity reasons). Fig.5 b) and c) show the charge density distribution of the CBM and the VBM containing only the Bi*6p*-Te*5p* and Te*5p*-Te*5p* contributions. This representation allows visualizing the orbital contributions of each atom to the CBM and VBM and hence provides a more detailed description of the band edges.

The main Bi*6p* and Te*5p* contributions to the CBM come from the Te2 and Bi2 atoms and those contributing to the VBM come from the Te3, Te4 and Te5 atoms. The Bi*6s* and Te*5s* states (*cf.* Fig. 6) are also important to obtain a more complete picture.

Fig. 6 COHP curves of $BaBiTe_3$ containing a) Bi-Te interactions and b) Te-Te interactions; c) shows a MO diagram reflecting the COHP analysis.

These mix with the Te*5p* states leading to significant contributions of Bi*6s*-Te*5p* antibonding states to the valence band edge. The conduction band edge also shows significant contributions of antibonding Bi*6p*-Te*5s* states. Our COHP analysis and the MO diagram (*cf.* Fig. 6) provide a comprehensive picture of all covalent bonding interactions in $BaBiTe_3$ and they show to which extent the different orbitals contribute to the electronic transport. However, Fig. 6 entirely neglects the ionic part of the crystal structure, which is not shown for clarity reasons. A detailed COHP analysis of the ionic part of the crystal structure can be found in the supplementary information and it shows significant contributions of the Ba*6s*-Te*5p* bonding states and Ba*5p*-Te*5p* antibonding states to the valence band edge.

Hence, a complete COHP analysis reveals that both the covalently and the ironically bonded parts as well as the Bi lone pairs of the crystal structure are expected to play a role in the electronic transport of $BaBiTe_3$.

Multiple electron pockets in the conduction band of Se substituted variants of $BaBiTe_3$

Optical absorption measurements of polycrystalline $BaBiTe_3$ (*cf.* Fig. 7a) confirm the results obtained for single crystalline $BaBiTe_3$ in 1997, which made it possible to use this compound as a standard for further optical absorption measurements of $BaBiTe_{2.95}Te_{0.05}$, $BaBiTe_{2.9}Se_{0.1}$ and $BaBiSe_3$ (*cf.* Fig. 7a).

Fig. 7 a) experimental band gaps of $BaBiTe_{3-x}Se_x$ (x = 0, 0.05, 0.1 and 3) determined by diffuse reflectance measurements; b) enlargement of the optical absorption of $BaBiTe_{2.95}Se_{0.05}$ emphasizing the two transitions corresponding to transitions from the VBM to CB_1 and from CB_1 to CB_2; c) energy of the two transitions as a function of the Se content; d) tauc plots for x = 0.05 showing that transition 2 can be considered direct.

These show that the optical band gap does not change significantly for compositions up to x = 0.1, while $BaBiSe_3$ has only one transition at ~0.90 eV (*cf.* Fig. 7a), which corresponds to an optical band gap significantly larger compared to those of $BaBiTe_{3-x}Se_x$ (x = 0, 0.05 and 0.1). The two optical transitions observed for $BaBiTe_3$ are also found for the Se substituted variants with x = 0.05 and 0.1 as it is illustrated in Fig. 7b for x = 0.05 and the energies of the two transitions are shown as a function of Se content in Fig. 7c.

Band convergence and an explanation for the two optical transitions

Up to now we provided a comprehensive picture of the bonding interactions in $BaBiTe_3$, its electronic structure including orbital contributions and we showed that $BaBiTe_{3-x}Se_x$ (x = 0, 0.05 and 0.1) are multiband systems. Now, we will relate the experimentally observed optical transitions to the electronic structure in order to explain the two optical transitions observed experimentally. These results are then used to demonstrate that band convergence occurs in $BaBiTe_{2.95}Se_{0.05}$.

Analyzing transition 2 of $BaBiTe_{2.95}Se_{0.05}$ by the Tauc method (*cf.* Fig. 7d) revealed that this transition is direct, which excludes the possibility of indirect VBM-CB_2 and VBM-CB_3 transitions being associated to transition 2. Fig. 8a shows the electronic structure and density of states (DOS) of $BaBiTe_3$ including two transitions, which can qualitatively explain the shape of the experimental absorption spectra shown in Fig. 7a and b.

Fig. 8 a) Electronic band structure and density of states (DOS) of $BaBiTe_3$ showing the two optical transitions taken into account for calculating the optical absorption spectrum; b) calculated joint density of states (joint DOS) and c) optical absorption coefficient as a function of energy. All these calculations were performed using DFT-PBE. The abbreviations T-1 and T-2 refer to transition 1 and transition 2.

This is also quantitatively validated in Fig. 8b and c presenting the calculated joint density of states and optical absorption spectrum of $BaBiTe_3$, respectively. These calculations were performed assuming that $BaBiTe_3$ is undoped (or has a very low carrier concentration). From these calculations we can conclude that transition 1 and 2 correspond to transitions from the VBM to CB_1 and to bands higher in the conduction band next to CB_2. These bands are located along the **ΓY** direction between CB_1 and CB_2 (*cf.* Fig. 8a).

Transition 2 is direct, which is consistent with the Tauc analysis shown in Fig. 7d. This transition is significantly stronger than transition 1 in terms of intensity. This can be explained by the lower dispersion of the bands higher in the conduction band compared to those at CB_1. A lower dispersion (i.e. when the bands are more flat) results in a larger density of states (*cf.* Fig. 8a). This is why the number of optical transitions at 0.26 eV (transition 1) is smaller than at 0.5 eV (transition 2). This is reflected in the joint density of states (*cf.* Fig. 8b), which are a measure for the amount of states in the valence and conduction band available for a photon of a given energy *hv* to interact with. The larger the available states, the higher is the transition rate and the larger is the intensity of the transition. Transition 2 is more intense than transition 1 since more states are available in the conduction band compared to transition 1.

High-temperature optical absorption measurements of $BaBiTe_{2.95}Se_{0.05}$ (*cf.* Fig. 9a) show that transition 2 moves to lower energies with respect to temperature, while the energy of transition 1 stays constant (*cf.* Fig. 9b).

Fig. 9 a) optical absorption spectra of $BaBiTe_{2.95}Se_{0.05}$ as a function of temperature b) changes in energy of transition 1 and 2 as a function of temperature; CB_1 and bands higher in the conduction band are converging with temperature; c) band offset as a function of Se content. This image shows that there is band convergence in $BaBiTe_{2.95}Se_{0.05}$ and that the band offset increases with the Se content.

Hence, the bands higher in the conduction band move towards lower energies. At ca. 830 K these bands can be considered as being fully converged with CB_1. Fig. 9c shows that the band offset between CB_1 and the bands higher in the conduction band (located along the **ΓY** direction between CB_1 and CB_2) slightly increases with the Se content. The band offset was extracted from the optical absorption measurements (*cf.* Fig. 7c).

Thermoelectric transport properties of $BaBiTe_{3-x}Se_x$ (x = 0, 0.05, 0.1)

The efficiency of a thermoelectric material is defined by the thermoelectric figure of merit (zT).

$$zT = \frac{S^2}{\rho\kappa}T \qquad (7)$$

The thermal conductivity (κ) contains the phononic (κ_{ph}), electronic (κ_e) and bipolar (κ_b) contribution. Seebeck coefficient (S), electrical resistivity (ρ) and the electronic and bipolar contribution of κ are interdependent, while κ_{ph} is mostly independent of the other quantities. The thermoelectric properties of polycrystalline $BaBiTe_{3-x}Se_x$ (x = 0, 0.05 and 0.1) are summarized in Fig. 10.

Fig. 10 Thermoelectric properties of $BaBiTe_{3-x}Se_x$ (x = 0, 0.05, 0.1): a) Seebeck coefficient (the dotted lines represent interpolated data), b) electrical resistivity, c) thermal conductivity and minimum thermal conductivity of $BaBiTe_3$ and $BaBiSe_3$ according to Cahill and d) thermoelectric figure of merit (zT).

Seebeck coefficient and thermal conductivity were measured out of plane, while the electrical resistivity was measured in plane. The Seebeck coefficient (*cf.* Fig. 10a) of all compounds increases up to ca. 550 K and shows a "roll-over" between 550 K and 600 K due to the activation of minority charge carriers. The maximum of the Seebeck coefficient (S_{max}) at the temperature T_{max} is almost independent of the Se content, which is consistent with the optical absorption spectra showing no significant changes in the optical band gap up to x = 0.1.

The Goldsmid-Sharp band gap ($E_g = 2eS_{max}T_{max}$) of all compounds measures ca. 0.23-0.25 eV, which agrees well with the optical band gap (0.26 eV).

Increasing the Se content leads to higher Seebeck coefficients, which is consistent with the increase in resistivity (*cf.* Fig. 10b). $BaBiTe_3$, $BaBiTe_{2.95}Se_{0.05}$ and $BaBiTe_{2.9}Se_{0.1}$ show a small reduction in thermal conductivity (*cf.* Fig. 10c) with an increasing Se content as expected from point defect scattering. This effect could also be due to the slightly different densities of the samples. However, because of the complex low symmetry structure (few acoustic phonons) and large anharmonicity the lattice thermal conductivity is already low (0.41(2) $Wm^{-1}K^{-1}$ at 600K). The thermal conductivity (not the diffusivity) of pristine $BaBiTe_3$ was previously measured on single crystals using a modified pulse technique originally developed by Maldonado.[16,54] The values we obtain for $BaBiTe_3$ using the Dulong Petit approximation compare well with the results published by Chung et al. (κ = 0.4 $Wm^{-1}K^{-1}$ for temperatures below ca. 150 K, where radiation effects due to insufficient heat dissipation can be neglected). It is therefore justifiable to use the Dulong-Petit approximation. All the title compounds possess remarkably low thermal conductivities close to the glass limit (*cf.* Fig. 10c) of $BaBiSe_3$ (0.34 $Wm^{-1}K^{-1}$) and $BaBiTe_3$ (0.28 $Wm^{-1}K^{-1}$). The glass limit is slightly higher for $BaBiSe_3$ since both, the longitudinal and transversal components of the speed of sound are larger for $BaBiSe_3$ (v_T = 1535 m/s, v_L = 2863 m/s) compared to $BaBiTe_3$ (v_T = 1462 m/s, v_L = 2536 m/s), which can be attributed to the

lower mass of Se compared to Te and to softer bonds in $BaBiSe_3$. Hence, $BaBiSe_3$ can be expected to be more anharmonic compared to $BaBiTe_3$. Fig. 11 shows the measured Hall mobility (μ) and charge carrier concentration (n) of $BaBiTe_{3-x}Se_x$ (x = 0, 0.05 and 0.1). The electron mobility (ranging from 2-5 $cm^2V^{-1}s^{-1}$) generally decreases temperature as expected from phonon scattering but may show grain boundary scattering at low temperature.

Fig.11 a) Hall mobility and b) hall charge carrier concentration of $BaBiTe_{3-x}Se_x$ (x = 0, 0.05, 0.1) as a function of temperature; c) calculated *zT* as a function of hall carrier concentration: lines and symbols correspond to effective band models and experimental data points, respectively; d) "Seebeck effective mass" (*m**) as a function of temperature (line and symbols represent calculated m* obtained from interpolated and experimental Seebeck data, respectively). b)-d) show the contribution of CB_2 for $BaBiTe_{3-x}Se_x$ (x = 0, 0.05) in form of an increase in carrier concentration and m* with temperature.

The carrier concentration of $BaBiTe_3$ is almost constant with temperature up to ca. 370 K and increases significantly between 370 K and 600 K like one might see from the formation of charged defects. A similar trend can be observed for $BaBiTe_{2.95}Se_{0.05}$. The increase in carrier concentration, however, is less pronounced and is only significant for temperatures above ca. 500 K.

Increasing the Se content further, results in an almost temperature independent carrier concentration for $BaBiTe_{2.9}Se_{0.1}$. The substitution of Te by Se does not affect the electron mobility in a systematic or significant way, but results in a clear reduction in charge carrier concentration. This decrease in carrier concentration with Se content explains the increase in resistivity. The possible origin for such high carrier concentrations will be discussed in the section: *Defect chemistry of $BaBiTe_3$ and its Se substituted variants*. The overall thermoelectric properties of $BaBiTe_3$ and $BaBiTe_{2.95}Se_{0.05}$ are fairly promising with zT_{max} (*cf.* Fig. 10d) of ~0.4.

Multiband effects in the thermoelectric transport properties of $BaBiTe_3$ and $BaBiTe_{2.95}Se_{0.05}$

Ab initio calculations of the electronic structure and optical absorption coefficient as well as optical absorption measurements clearly point towards a contribution of multiple electron pockets to the thermoelectric transport properties of $BaBiTe_{3-x}Se_x$, especially at higher temperatures where band convergence effects play a role (*cf.* Fig. 9). A comparison of this study to those of SnSe[52] and $CoSb_3$[53], where multiband effects also play a role, support this conclusion. We indeed find a multiband contribution to the thermoelectric transport data of $BaBiTe_3$ and $BaBiTe_{2.95}Se_{0.05}$. It is visible in the increase of the "Seebeck effective mass" (m*)[53] with temperature (*cf.* Fig. 11c), as obtained by fitting an effective band model to the experimental data (*cf.* Fig. 11d), where Seebeck coefficient and resistivity show the typical trends of degenerate semiconductors. Details concerning modeling of high-temperature thermoelectric properties can be found elsewhere.[55] The main signature of multiband effects in the transport data is an increase in effective mass with decreasing Se content (*cf.* Fig. 11c), while the hall mobility remains almost unchanged. Another signature of multiband effects in the thermoelectric transport data is the lower effective mass of Se-alloyed $BaBiTe_{2.95}Se_{0.1}$ compared to $BaBiTe_3$. This suggests that for $BaBiTe_{2.9}Se_{0.1}$ only CB_1 contributes to the thermoelectric transport, while the bands along the **ΓY** direction between CB_1 and CB_2 contribute in the case of $BaBiTe_3$ since the "Seebeck effective mass" is an estimate for the effective density of states. The previously discussed convergence of bands in the conduction band on the other hand can explain the increase in effective mass with temperature, which is only observed for $x = 0$ and 0.05. One possible explanation for not observing any effect of band convergence on the thermoelectric transport properties of $BaBiTe_{2.9}Se_{0.1}$ is the increase in band offset with x, which could also explain the weaker increase

in effective mass for x=0.05 compared to x = 0 and the absence of the low-energy optical transition in $BaBiSe_3$ (*cf.* Fig. 7a). Our combined analyses of the electronic structure, optical properties and thermoelectric transport properties strongly suggest that the larger quality factor (B) and zT_{max} of x = 0 and 0.05 compared to $BaBiTe_{2.9}Se_{0.1}$ (*cf.* Fig. 11d) are a result of the multiband and band convergence effects. B was calculated according to (8), where m_e and κ_{ph} are the electron mass and phononic contribution to the thermal conductivity.

$$B = 4.3223 * 10^{-6}\ \mu_0 \left(\frac{m^*}{m_e}\right)^{3/2} \frac{T^{5/2}}{\kappa_{ph}} \qquad (8)$$

The intrinsic mobility (μ_0) and effective mass (m^*) were obtained from the effective band model. Fitting such a model to the thermoelectric transport data also shows that the carrier concentration of all title compounds is close to optimized (*cf.* Fig. 11d).

Defect chemistry of $BaBiTe_3$ and its Se substituted variants

The main reason for studying the defect chemistry of $BaBiTe_{3-x}Se_x$ is the large charge carrier concentration observed, which points towards unintentional doping through native defects. The closely related to Bi_2Te_3, Bi_2Se_3 and their solid solutions also have native defects that play an important role in their thermoelectric transport properties.[56-61] Insights in the defect chemistry can help to explain, why $BaBiTe_3$ and its Se substituted variants are all n-type semiconductors and possibly predict whether intrinsic p-type samples can be obtained. We calculated the formation energies ($E_f[D^q]$) of intrinsic defects in $BaBiTe_3$ in three different regions of the Ba-Bi-Te phase diagram (*cf.* Fig. 12).

Fig. 12 Formation energies of intrinsic defects in $BaBiTe_3$ calculated in three different regions of the Ba-Bi-Te phase diagram: a) region 1: BaTe-Bi_2Te_3-$BaBiTe_3$, b) region 2: BaTe-Te-$BaBiTe_3$ and c) region 3: Bi_2Te_3-Te-$BaBiTe_3$; the numbers in each graph correspond to the charge q of the each type of defect. These calculations reveal native Bi_{Ba}^{+1} defects with negative defect formation energies close to the valence band edge in all three regions of the phase diagram. These defects are competing with native Te_{Bi}^{+1} defects in the region 2 (b) of the phase diagram for energies close to the valence band edge; these calculations were performed using DFT-PBE.

The values of allowed chemical potential are determined by the three regions BaTe-Bi_2Te_3-$BaBiTe_3$, BaTe-Te-$BaBiTe_3$ and Bi_2Te_3-Te-$BaBiTe_3$, which will be referred to as region (*a*), (*b*), and (*c*). These different regions correspond to different thermodynamic conditions in which $BaBiTe_3$ is stable and are related to different synthesis conditions.[62] Figure 12 plots the defect formation energy depending on the Fermi level for a series of intrinsic defects in different regions of chemical potential. In all conditions, there are Bi_{Ba}^{+1} and Te_{Bi}^{+1} defects with negative formation energies close to the valence band maximum. These defects are electron donors compensating any attempt to dope the material p-type in equilibrium conditions. On the other hand, no negative formation energy defects are present close to the conduction band minimum indicating that the material has no electron killers. We conclude that $BaBiTe_3$ is thermodynamically favoring n-type conductivity and that any attempt to dope this material p-type will be challenging. This is in agreement with the n-type nature of the experimentally realized materials. Moreover, our work identifies the potential majority defects, Bi_{Ba}^{+1}, which are the lowest energy electron donors in all regions, probably leading to the observed n-type conduction.

In $BaBiTe_3$ a second cation (Ba^{2+}) is present, which is lacking in Bi_2Te_3 and which fundamentally changes the defect chemistry since antisite defects form more easily between two cations than between a cation and an anion. This is evident from the low formation energy of the Bi_{Ba}^{+1} antisite defects in $BaBiTe_3$. In n-type Bi_2Te_3 and Bi_2Se_3 Te_{Bi}^{+1}, Se_{Bi}^{+1} (under Se-rich

conditions) and V_{Se}^{2+} (under Bi-rich conditions) defects have the lowest formation energies and are responsible for the observed n-type conduction in these compounds.[56] The vacancies of Te and Se are also low in energy in Bi_2Te_3, while being much higher in energy than Bi_{Ba}^{+1} in $BaBiTe_3$. Interestingly, Bi_2Te_3 can easily be doped p- and n-type, while p-type doping of $BaBiTe_3$ is challenging due to the low formation energies of the Bi_{Ba}^{+1} antisite defects.

Our defect calculations show that the defect chemistry of $BaBiTe_3$ differs significantly from the one in Bi_2Te_3 and the reason for the difference is the presence of Ba^{2+} as a second cation. The preferential site substitution of Se on the Te4 and Te5 sites presented above (*cf.* section: *Preferential site substitution of Se on the Te4 and Te5 sites*) motivated us to study the defect chemistry of Se substituted variants of $BaBiTe_3$ in order to explain this preference from an energetic point of view. Results of our extrinsic defect calculations can be found in the supplementary information and they revealed equally low formation energies close to zero for Se_{Te4} and Se_{Te5} defects, which explain the preferential site substitution on the Te4 and Te5 sites.

Conclusion

The presence of Te···Te resonant bonds in $BaBiTe_3$ is best described as a linear combination of interdigitating $(Te^{1-})_2$ side groups and infinite Te_n chains. Complementary Rietveld refinements and extrinsic defect calculations show that the Se substitution preferentially occurs on the Te4 and Te5 sites, which are not involved in Te···Te bonding. Ab initio calculations of the electronic structure, optical absorption measurements and an effective band model analysis of the thermoelectric transport properties of $BaBiTe_{3-x}Se_x$ (x = 0, 0.05 and 0.1) strongly suggest the presence of multiple conduction bands. These analyses also provide an explanation for the two optical transitions observed experimentally. Bands higher in the conduction band converge with the conduction band minimum with increasing temperature and contribute to the thermoelectric

transport properties of $BaBiTe_3$ and $BaBiTe_{2.95}Se_{0.05}$. This multiband contribution can be considered as the reason for the ~50 % higher zT at 617 K compared to $BaBiTe_{2.9}Se_{0.1}$, for which no such contribution was found. The increase in the band offset between the CBM and bands higher in the conduction band with respect to the selenium content is one possible explanation for the absence of multiband effects in the thermoelectric transport properties of $BaBiTe_{2.9}Se_{0.1.}$

A detailed analysis of the defect chemistry of $BaBiTe_3$ suggests the presence of native Bi_{Ba}^{+1} and Te_{Bi}^{+1} defects at 0 K and these are probably responsible for the observed n-type conduction. $BaBiTe_3$ is the first example of a mixed-valent chalcogenide with Te···Te resonant bonds, where its thermoelectric properties benefit from the contribution of multiple conduction bands. Hence, chalcogenides with resonant bonds are promising for continued investigations as new thermoelectric materials.

Acknowledgements

The authors thank Riley Hanus for his support concerning the measurement and evaluation of the speed of sound. Financial support from the 2016 ITS Summer Fellowship awarded by the International Thermoelectric Society is gratefully acknowledged. The authors acknowledge financial support from the french "Agence Nationale de la Recherche" (ANR) through the program "Investissements d'Avenir"(ANR-10-LABX-09-01), LabEx EMC3. This work made use of the EPIC facility of the NUANCE Center at Northwestern University, which has received support from the Soft and Hybrid Nanotechnology Experimental (SHyNE) Resource (NSF NNCI-1542205); the MRSEC program (NSF DMR-1121262) at the Materials Research Center; the International Institute for Nanotechnology (IIN); the Keck Foundation; and the State of Illinois, through the IIN. MGK is supported by a grant by the U.S. Department of Energy, Office of Science, and Office of Basic Energy Sciences under the Award Number DE-SC0014520 (electronic structure calculations, sample measurements, characterization). G. Y., G. H. and G.-

M. R. acknowledge financial support from the F.R.S.-FNRS project HTBaSE (contract no PDR-T.1071.15). V.-A. H. was funded through a grant from the FRIA. Computational resources were provided by the supercomputing facilities of the Université catholique de Louvain (CISM/UCL), the Consortium des Equipements de Calcul Intensif en Fédération Wallonie Bruxelles (CECI) funded by the F.R.S.-FNRS.

Supporting information

Details on speed of sound measurements and evaluation of ω_D and θ_D

EDS spectra of all title compounds

Results of extrinsic defect calculations

Electronic structure calculations

COHP curves containing all Ba-Te interactions

Thermal diffusivities of $BaBiTe_{3-x}Se_x$ (x = 0, 0.05 and 0.1)

References

(1) Sheldrick, W. S. Polychalcogenide Anions: Structural Diversity and Ligand Versatility. *Z. Anorg. Allg. Chem.* **2012**, *638*, 2401-2424.

(2) Mayasree, O.; Sankar, C. R.; Kleinke, K. M.; Kleinke, H. Cu clusters and chalcogen-chalcogen bonds in various copper polychalcogenides. *Coord. Chem. Rev.* **2012**, *256*, 1377-1383.

(3) Böttcher, P. Tellurium-Rich Tellurides. *Angew. Chem. Int. Ed. Engl.* **1988**, *27*, 759-772.

(4) Mrotzek, A.; Kanatzidis, M. G. "Design" in solid-state chemistry based on phase homologies. The concept of structural evolution and the new megaseries A(m)[M1+1Se2+1](2m)[M21+nSe2+31+n] *Acc. Chem. Res.* **2003,** *36*, 111-119.

(5) Lin, H.; Tan, G. J.; Shen, J. N.; Hao, S. Q.; Wu, L. M.; Calta, N.; Malliakas, C.; Wang, S.; Uher, C.; Wolverton, C.; Kanatzidis, M. G. Concerted rattling in $CsAg_5Te_3$ leading to ultralow thermal conductivity and high thermoelectric performance. *Angew. Chem. Int. Ed.* **2016,** *55*, 11431-11436.

(6) Pei, Y.; Chang, C.; Wang, Z.; Yin, M.; Wu, M.; Tan, G.; Wu, H.; Chen, Y.; Zheng, L.; Gong, S.; Zhu, T.; Zhao, X.; Huang, L.; He, J.; Kanatzidis, M. G.; Zhao, L.-D. Multiple converged conduction bands in $K_2Bi_8Se_{13}$: A promising thermoelectric material with extremely low thermal conductivity. *J. Am. Chem. Soc.*, **2016**, *138*, 16364-16371.

(7) Lowhorn, N. D.; Tritt, T. M.; Abbott, E. E.; Kolis, J. W. Enhancement of the power factor of the transition metal pentatelluride $HfTe_5$ by rare-earth doping. *Appl. Phys. Lett.*, **2006**, *88*, 022101(1-3).

(8) Assoud, A.; Thomas, S.; Sutherland, B.; Zhang, H.; Tritt, T. M.; Kleinke, H. Thermoelectric properties of the new polytelluride $Ba_3Cu_{14-\delta}Te_{12}$. *Chem. Mater.*, **2006**, *18*, 3866-3872.

(9) Mayasree, O.; Sankar, C. R.; Cui, Y.; Assoud, A.; Kleinke, H. Synthesis, structure and thermoelectric properties of barium copper polychalcogenides with chalcogen-centered Cu clusters and Te_2^{2-} dumbbells. *Eur. J. Inorg. Chem.*, **2011**, *26*, 4037-4042.

(10) Patschke, R.; Zhang, X.; Singh, D.; Schindler, J.; Kannewurf, C. R.; Lowhorn, N.; Tritt, T.; Nolas, G. S.; Kanatzidis, M. G. Thermoelectric properties and electronic structure of the cage compounds $A_2BaCu_8Te_{10}$ (A = K, Rb, Cs): Systems with low thermal conductivity. *Chem. Mater.* **2001,** *13*, 613-621.

(11) Mahan, G. D. *Solid State Physics*; Academic Press: San Diego, 1998.

(12) Goldsmid, H. J. *Thermoelectric Refrigeration*; Springer: New York, 1964.

(13) Pei, Y.; Shi, X.; LaLonde, A.; Wang, H.; Chen, L.; Snyder, G. J. Convergence of electronic bands for high performance bulk thermoelectrics. *Nature*, **2011**, *473*, 66-69.

(14) Chasapis, T. C.; Lee, Y.; Hatzikraniotis, E.; Paraskevopoulos, K. M.; Chi, H.; Uher, C.; Kanatzidis, M. G. Understanding the role and interplay of heavy-hole and light-hole valence bands in the thermoelectric properties of PbSe. *Phys. Rev. B*, **2015**, *91*, 085207(1-11).

(15) Volk, K.; Cordier, G.; Cook, R.; Schäfer, H. $BaSbTe_3$ and $BaBiSe_3$ – Compounds with BiSe-layer or SbTe-layer structures, respectively. *Z. Naturforsch.*, **1980**, *35b*, 136-140.

(16) Chung, D.-Y.; Jobic, S.; Hogan, T.; Kannewurf, C. R.; Brec, R.; Rouxel, J.; Kanatzidis, M. G. Oligomerization versus polymerization of Te_x^{n-} in the polytelluride compound $BaBiTe_3$. Structural characterization, electronic Structure, and thermoelectric properties. *J. Am. Chem. Soc.*, **1997**, *119*, 2505-2515.

(17) Slack, G. A. *New Materials and Performance Limits for Thermoelectric Cooling* in *CRC Handbook of Thermoelectrics*; CRC Press: Florida, 1995.

(18) Takahashi, H.; Raghavendra, N.; Gascoin, F.; Pelloquin, D.; Hébert, S.; Guilmeau, E. Transport properties of an intermetallic with pseudo-hollandite structure as potential thermoelectric material: The example of $Tl_xCr_5Se_8$. *Chem. Mater.*, **2013**, *25*, 1809-1815.

(19) Lefèvre, R.; Berthebaud, D.; Perez, O.; Pelloquin, D.; Hébert, S.; Gascoin, F. Polar Transition-Metal Chalcogenide: Structure and Properties of the New Pseudo-Hollandite $Ba_{0.5}Cr_5Se_8$. *Chem. Mater.* **2015**, *27*, 7110-7118.

(20) Maier, S.; Lefèvre, R.; Lin, X.; Raghavendra, N.; Berthebaud, D.; Hébert, S.; Mar, A.; Gascoin, F. The solid solution series $Tl(V_{1-x}Cr_x)_5Se_8$: crystal structure, magnetic and thermoelectric properties. *J. Mater. Chem. C*, **2015**, *3*, 10509-10517.

(21) Suekuni, K.; Yakasu, Y.; Hasegawa, T.; Ogita, N.; Udagawa, M.; Avila, M. A.; Takabatake, T. Off-center rattling modes and glasslike thermal conductivity in the type-I clathrate $Ba_8Ga_{16}Sn_{30}$. *Phys. Rev. B*, **2010**, *81*, 205207(1-5).

(22) Christensen, M.; Iversen, B. B. Host structure engineering in thermoelectric clathrates. *Chem. Mater.*, **2007**, *19*, 4896-4905.

(23) Maier, S.; Perez, O.; Pelloquin, D.; Berthebaud, D.; Hébert, S.; Gascoin, F. Linear, hypervalent Se_3^{4-} units and unprecedented Cu_4Se_9 building blocks in the copper(I) selenide $Ba_4Cu_8Se_{13}$. *Inorg. Chem.* **2017**, *56*, 9209-9218.

(24) Nielsen, M. D.; Ozolins, V.; Heremans, J. P. Lone pair electrons minimize lattice thermal conductivity. *Energy Environ. Sci.*, **2013**, *6*, 570-578.

(25) Petrov, A. V.; Shtrum, E. L. Heat conductivity and the chemical bond in ABX_2 compounds. *Sov. Phys. Solid State*, **1962**, *4*, 1061-1065.

(26) Morelli, D. T.; Jovovic, V.; Heremans, J. P. Intrinsically minimal thermal conductivity in cubic I-V-VI_2 semiconductors. *Phys. Rev. Lett.*, **2008**, *101*, 035901(1-4).

(27) Skoug, E. J.; Morelli, D. T. Role of lone-pair electrons in producing minimum thermal conductivity in nitrogen-group chalcogenide compounds. *Phys. Rev. Lett.*, **2011**, *107*, 235901(1-5).

(28) Larson, P.; Mahanti, S. D.; Kanatzidis, M. G. Electronic structure and transport of Bi2Te3 and $BaBiTe_3$. *Phys. Rev. B*, **2000**, *61*, 8162-8171.

(29) Meng, J. F.; Shekar, N. V. C.; Badding, J. V.; Chung, D.-Y.; Kanatzidis, M. G. Multifold enhancement of the thermoelectric figure of merit in p-type $BaBiTe_3$ by pressure tuning. *J. Appl. Phys.*, **2001**, *90*, 2836-2839.

(30) Zhou, Y.; Zhao, L.-D. Thermoelectric transport properties of $BaBiTe_3$-based materials. *J. Solid State Chem.*, **2017**, *249*, 131-135.

(31) Rodriguez-Carvajal, J. Recent advances in magnetic structure determination by neutron powder diffraction + Fullprof. *Physica B*, **1993**, *192*, 55-56.

(32) Borup, K. A.; De Boor, J.; Wang, H.; Drymiotis, F.; Gascoin, F.; Shi, X.; Chen, L.; Fedorov, M. I.; Müller, E.; Iversen, B. B.; Snyder, G. J. Measuring thermoelectric transport properties of materials. *Energy Environ. Sci.*, **2015**, *8*, 423-435.

(33) Iwanaga, S.; Toberer, E. S.; LaLonde, A.; Snyder, G. J. A high temperature apparatus for measurement of the Seebeck coefficient. *Rev. Sci. Instrum.*, **2011**, *82*, 063905(1-6).

(34) Truell, R.; Elbaum, C.; Chick, B. B. *Ultrasonic Methods in Solid State Physics*; Academic Press: New York, 1969.

(35) Cahill, D. G.; Watson, S. K.; Pohl, R. O. Lower limit of the thermal conductivity of disordered crystals. *Phys. Rev. B*, **1992**, *46*, 6131-6140.

(36) Kresse, G. thesis, Technische Universität Wien, 1993.

(37) Kresse, G.; Hafner, J. Ab-initio molecular dynamics for open-shell transition metals. *Phys. Rev. B* **1993**, *13*, 13115-13118.

(38) Kresse, G.; Hafner, J. Norm-conserving and ultrasoft pseudopotentials for first-row and transition elements. *J. Phys.Condens. Matter* **1994**, *6*, 8245-8257.

(39) Kresse, G.; Furthmüller, J. Efficiency of ab-initio total energy calculations for metals and semiconductors using a plane-wave basis set. *Comput. Mater. Sci.* **1996**, *6*, 15-50.

(40) Blöchl, P. E. Projector augmented-wave method. *Phys. Rev. B*, **1994**, *50*, 17953-17979.

(41) Perdew, J. P.; Burke, K.; Ernzerhof, M. Generalized gradient approximation made simple. *Phys. Rev. Lett.*, **1996**, *77*, 3865-3868.

(42) Maintz, S.; Deringer, V. L.; Tchougréeff, A. L.; Dronskowski, R. LOBSTER: A tool to extract chemical bonding from plane-wave based DFT. *J. Comput. Chem.*, **2016**, *37*, 1030-1035.

(43) Freysoldt, C.; Grabowski, B.; Hickel, T.; Neugebauer, J.; Kresse, G.; Janotti, A.; Van de Walle, C. G. First-principles calculations for point defects in solids. *Rev. Mod. Phys.*, **2014**, *86*, 253-305.

(44) Taylor, S. E.; Bruneval, F. Understanding and correcting the spurious interactions in charged supercells. *Phys. Rev. B*, **2011**, *84*, 075155(1-8).

(45) Jain, A.; Ong, S. P.; Hautier, G.; Chen, W.; Richards, W. D.; Dacek, S.; Cholia, S.; Gunter, D.; Skinner, D.; Ceder, G.; Persson, K. A. Commentary: The Materials Project: A materials genome approach to accelerating materials innovation. *APL Mater.* **2013**, *1*, 11002(1-11).

(46) Ong, S. P.; Richards, W. D.; Jain, A.; Hautier, G.; Kocher, M.; Cholia, S.; Gunter, D.; Chevrier, V. L.; Persson, K. A.; Ceder, G. Python Materials Genomics (pymatgen): A robus, open-source python library for materials analysis. *Comput. Mater. Sci.*, **2013**, *68*, 314-319.

(47) Freysoldt, C.; Neugebauer, J.; Van de Walle, C. G. Fully ab initio finite-size corrections for charged-defect supercell calculations. *Phys. Rev. Lett.*, **2009**, *102*, 016402(1-4).

(48) Kumagai, Y.; Oba, F. Electrostatics-based finite-size corrections for first-principles point defect calculations. *Phys. Rev. B*, **2014**, *89*, 195205(1-15).

(49) Ha, V.-A.; Waroquiers, D.; Rignanese, G.-M.; Hautier, G. Influence of the "second gap" on the transparency of transparent conducting oxides: An ab initio study. *Appl. Phys. Lett.*, **2016**, *108*, 201902(1-5).

(50) Pauling, L. *Nature of The Chemical Bond*; Cornell University Press: Ithaca, 1960.

(51) Chauvin, R. Explicit periodic trend of van der Waals radii. *J. Phys. Chem.*, **1992**, *96*, 9194-9197.

(52) Zhao, L.-D.; Tan, G.; Hao, S.; He, J.; Pei, Y.; Chi, H.; Wang, H.; Gong, S.; Xu, H.; Dravid, V. P.; Uher, C.; Snyder, G. J.; Wolverton, C.; Kanatzidis, M. G. Ultrahigh power factor and thermoelectric performance in hole-doped single-crystal SnSe. *Science* **2016**, *351*, 141-144.

(53) Tang, Y.; Gibbs, Z. M.; Agapito, L. A.; Li, G.; Kim, H.-S.; Nardelli, M. B.; Curtarolo, S.; Snyder, G. J. Convergence of multi-valley bands as the electronic origin of high thermoelectric performance in $CoSb_3$ skutterudites. *Nat. Mater.*, **2015**, *14*, 1223-1228.

(54) Maldonado, O. Pulse method for simultaneous measurement of electric thermopower and heat conductivity at low temperatures. *Cryogenics,* **1992**, *32*, 908-912.

(55) May, A. F.; Snyder G. J. *Introduction to Modeling Thermoelectric Transport at High Temperatures* in *Materials, Preparation and Characterization in Thermoelectrics*; CRC Press: Florida, 2012.

(56) Scanlon, D. O.; King, P. D. C.; Singh, R. P.; De la Torre, A.; McKeown Walker, S.; Balakrishnan, G.; Baumberger, F.; Catlow, C. R. A. Controlling bulk conductivity in topological insulators: Key role of anti-site defects. *Adv. Mater.*, **2012**, *24*, 2154-2158.

(57) Wu, K. K.; Ramachandran, B.; Kuo, Y. K.; Sankar, R.; Chou, F. C. Influence of induced defects on transport properties of the Bridgman-grown Bi_2Se_3-based single crystals. *J. Alloy. Compd.*, **2016**, *682*, 225-231.

(58) Bedoya-Martinez, O. N.; Hashibon, A.; Elsässer, C. Influence of point defects on the phonon thermal conductivity and phonon density of states of Bi_2Te_3. *Phys. Status Solidi A*, **2016**, *3*, 684-693.

(59) Wang, L.-L.; Huang, M.; Thimmaiah, S.; Alam, A.; Bud'ko, S. L.; Kaminski, A.; Lograsso, T. A.; Canfield, P.; Johnson, D. D. Native defects in tetradymite $Bi_2(Te_xSe_{3-x})$ topological insulators. *Phys. Rev. B*, **2013**, *87*, 125303(1-6).

(60) Zhu, T.; Hu, L.; Zhao, X.; He, J. New insights into intrinsic point defects in V_2VI_3 thermoelectric materials. *Adv. Sci.*, **2016**, *3*, 1600004(1-16).

(61) Suh, J.; Yu, K. M.; Liu, X.; Yang, F.; Fan, J.; Smith, D. J.; Zhang, Y.-H.; Furdyna, J. K.; Dames, C.; Walukiewicz, W.; Wu, J. Simultaneous enhancement of electrical conductivity and thermopower of Bi_2Te_3 by multifunctionality of native defects. *Adv. Mater.*, **2015**, *27*, 3681-3686.

(62) Ohno, S.; Aydemir, U.; Amsler, M.; Pöhls, J.-H.; Chanakian, S.; Zevalkink, A.; White, M. A.; Bux, S. K.; Wolverton, C.; Snyder, G. J. Achieving zT > 1 in inexpensive Zintl phase $Ca_9Zn_{4+x}Sb_9$ by Phase Boundary Mapping. *Adv. Funct. Mater.* **2017**, *27*, 1606361(1-10).

TOC figure:

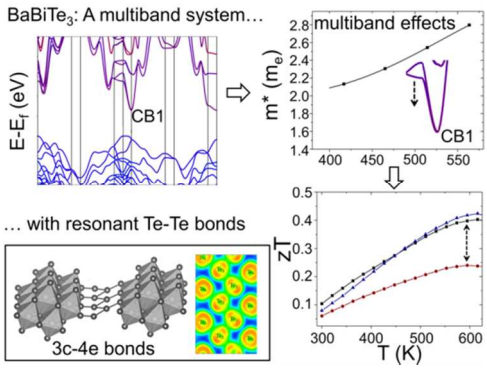
BaBiTe3: A multiband system…
E-Ef (eV)
CB1
multiband effects
m* (me)
CB1
… with resonant Te-Te bonds
3c-4e bonds
zT
T (K)

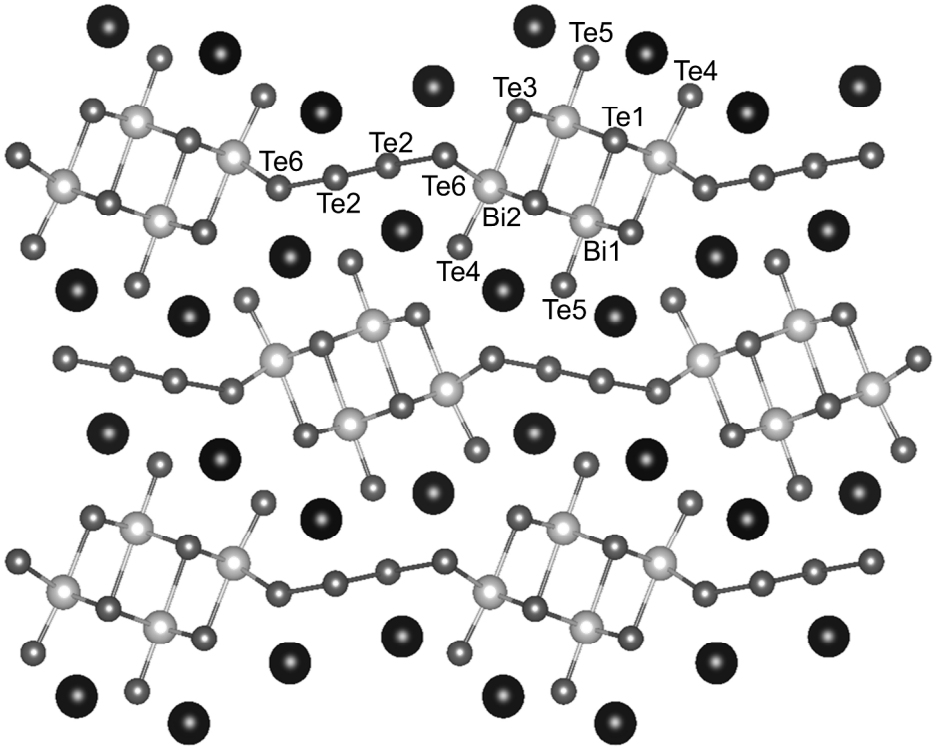

Crystal structure of BaBiTe3 (black: Ba, light grey: Bi, dark grey: Te)

254x190mm (300 x 300 DPI)

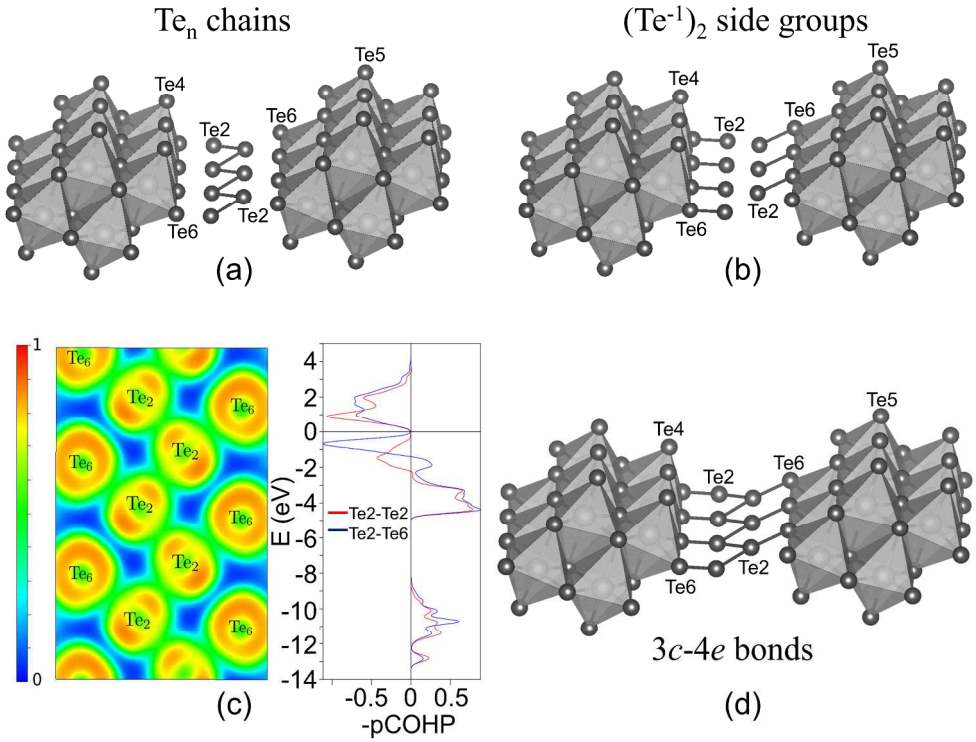

Previously described Te···Te bonding situations: a) Ten chains and b) interdigitating (Te1-)2 side groups; c) electron localization function of Te2 and Te6 (left) and -pCOHP curves of the Te2-Te2 and Te2-Te6 pairs (right) showing bonding interactions between Te2-Te2 and Te2-Te6; d) resonant Te···Te bonding, which can be understood as a linear combination between a) and b) and which involves three-center-four-electron (3c-4e) bonds; the bonding situation in d) is based on results from –pCOHP and ELF calculations shown in c); this new Te···Te bonding situation represents an electron delocalization over the Te2 and Te6 atoms, which reduces electrostatic repulsion between the Te2 and the Te6 atoms by minimizing their negative charge.

254x190mm (300 x 300 DPI)

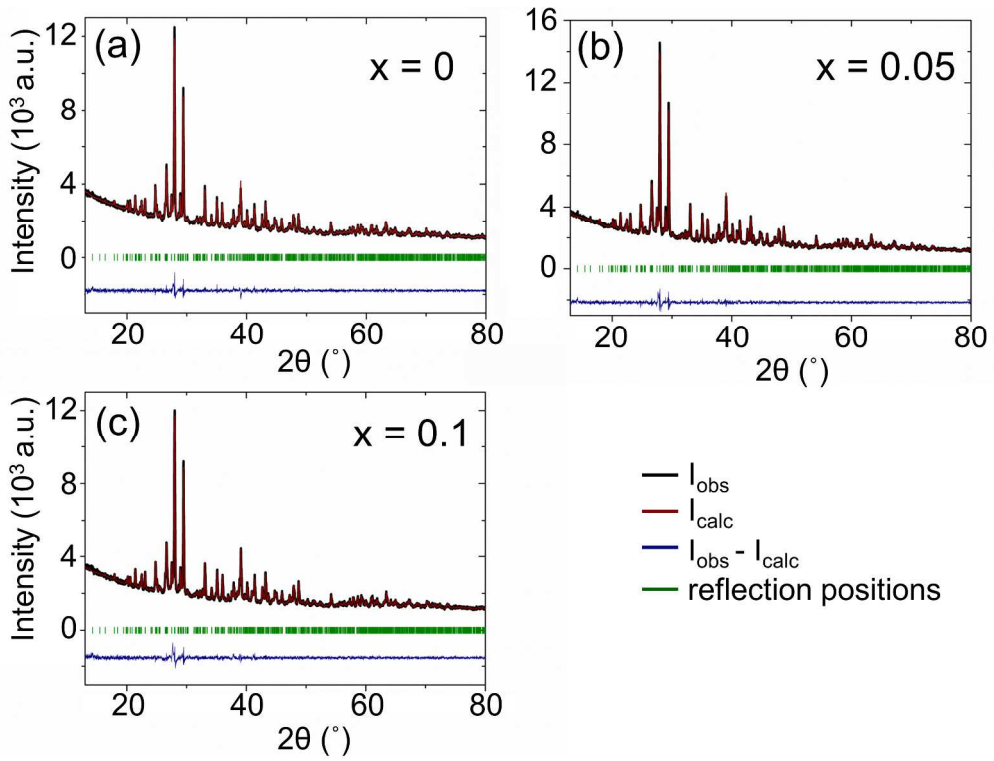

Rietveld refinements of experimental diffraction patterns (black) of a) BaBiTe3, b) BaBiTe2.95Se0.05 and c) BaBiTe2.9Se0.1 recorded after spark plasma sintering. Calculated diffraction patterns, difference plots and reflection positions are depicted in red, blue and green, respectively; all experimental diffraction patterns were recorded after spark plasma sintering.

254x190mm (300 x 300 DPI)

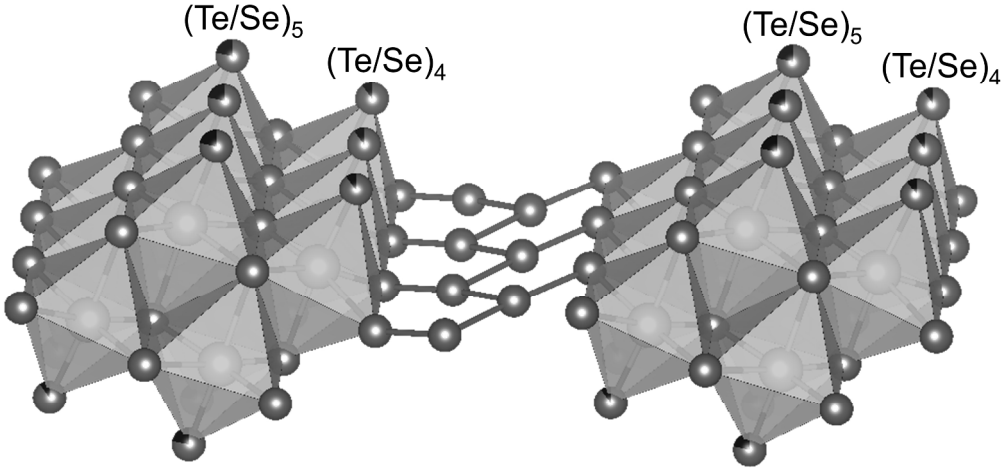

Parts of the BaBiTe2.9Se0.1 crystal structure with refined site occupancy factors (black: Se; grey: Te) illustrating the preferential site substitution of Te4 and Te5 by Se.

254x190mm (300 x 300 DPI)

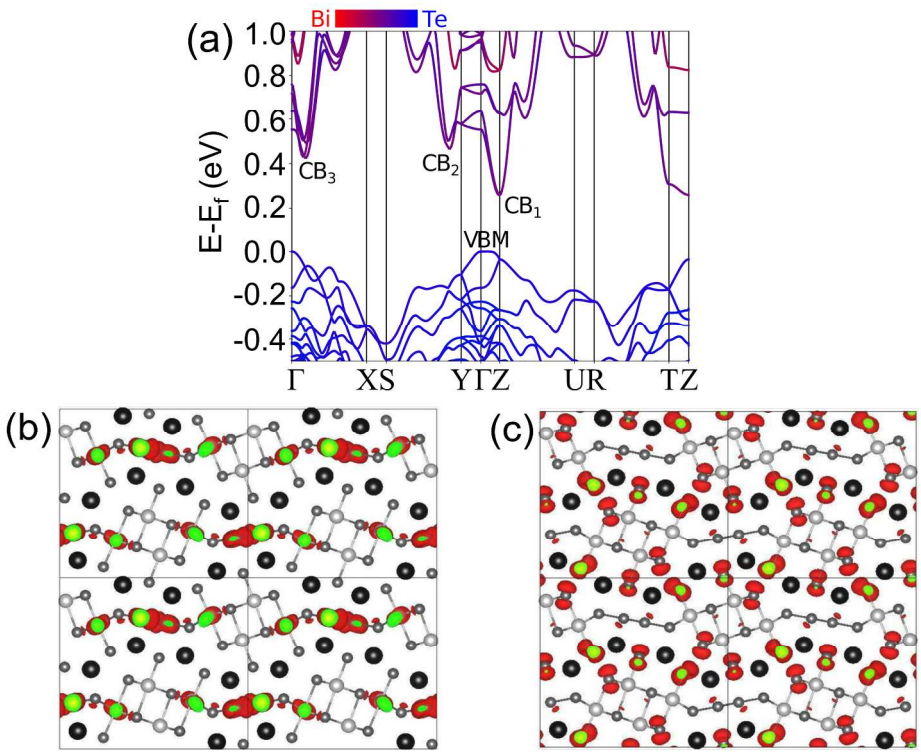

a) Electronic structure of BaBiTe3 with three electron pockets (CB1, CB2 and CB3) and the atomic contributions to the conduction band minimum (CBM) and valence band maximum (the Fermi level is set to 0 eV); b) and c) correspond to the charge density distribution of the CBM and the valence band maximum (VBM) showing the strongest atomic contributions to the CBM and VBM; all calculations were performed using DFT-PBE.

254x190mm (300 x 300 DPI)

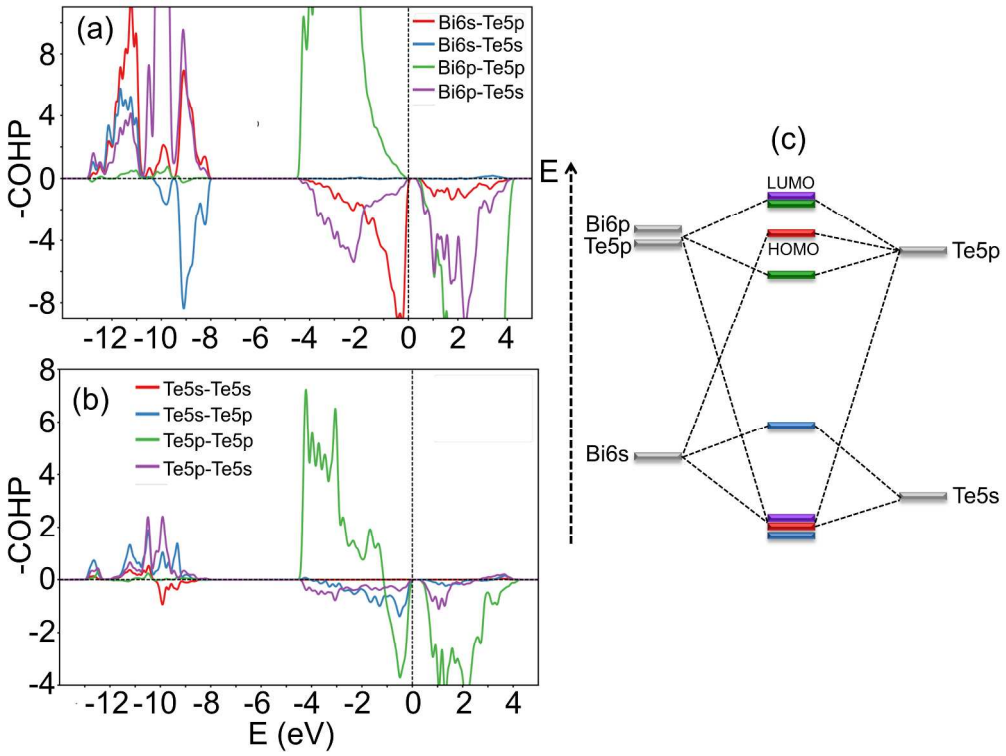

COHP curves of BaBiTe3 containing a) Bi-Te interactions and b) Te-Te interactions; c) shows a MO diagram reflecting the COHP analysis.

254x190mm (300 x 300 DPI)

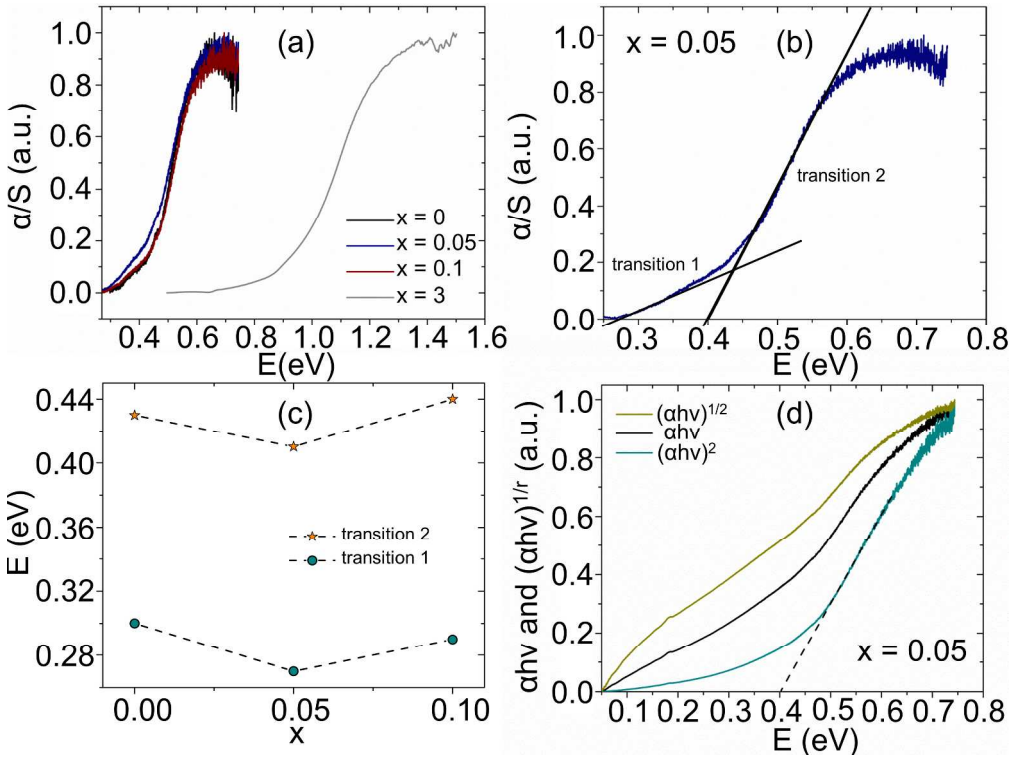

a) experimental band gaps of BaBiTe3-xSex (x = 0, 0.05, 0.1 and 3) determined by diffuse reflectance measurements; b) enlargement of the optical absorption of BaBiTe2.95Se0.05 emphasizing the two transitions corresponding to transitions from the VBM to CB1 and from CB1 to CB2; c) energy of the two transitions as a function of the Se content; d) tauc plots for x = 0.05 showing that transition 2 can be considered direct.

254x190mm (300 x 300 DPI)

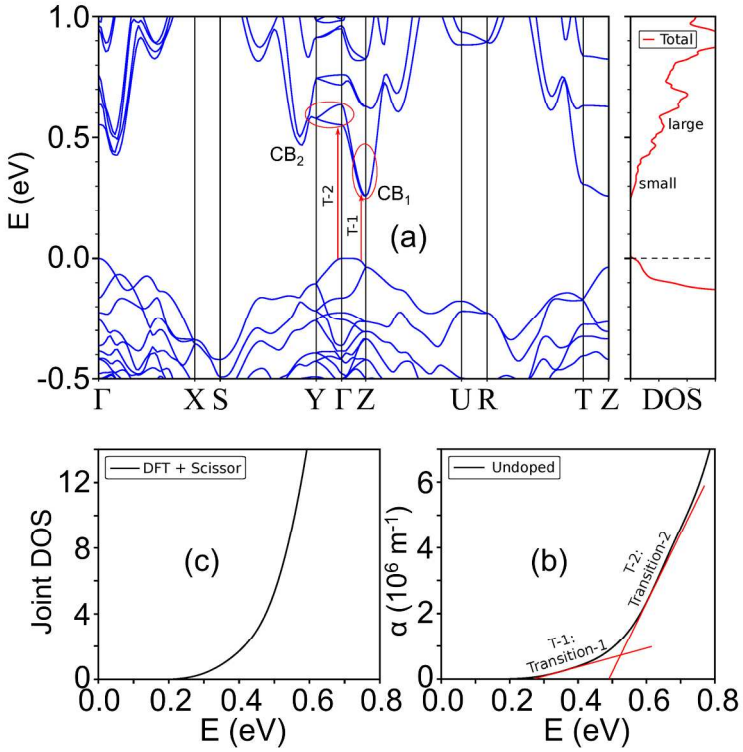

a) Electronic band structure and density of states (DOS) of BaBiTe3 showing the two optical transitions taken into account for calculating the optical absorption spectrum; b) calculated joint density of states (joint DOS) and c) optical absorption coefficient as a function of energy. All these calculations were performed using DFT-PBE. The abbreviations T-1 and T-2 refer to transition 1 and transition 2.

254x190mm (300 x 300 DPI)

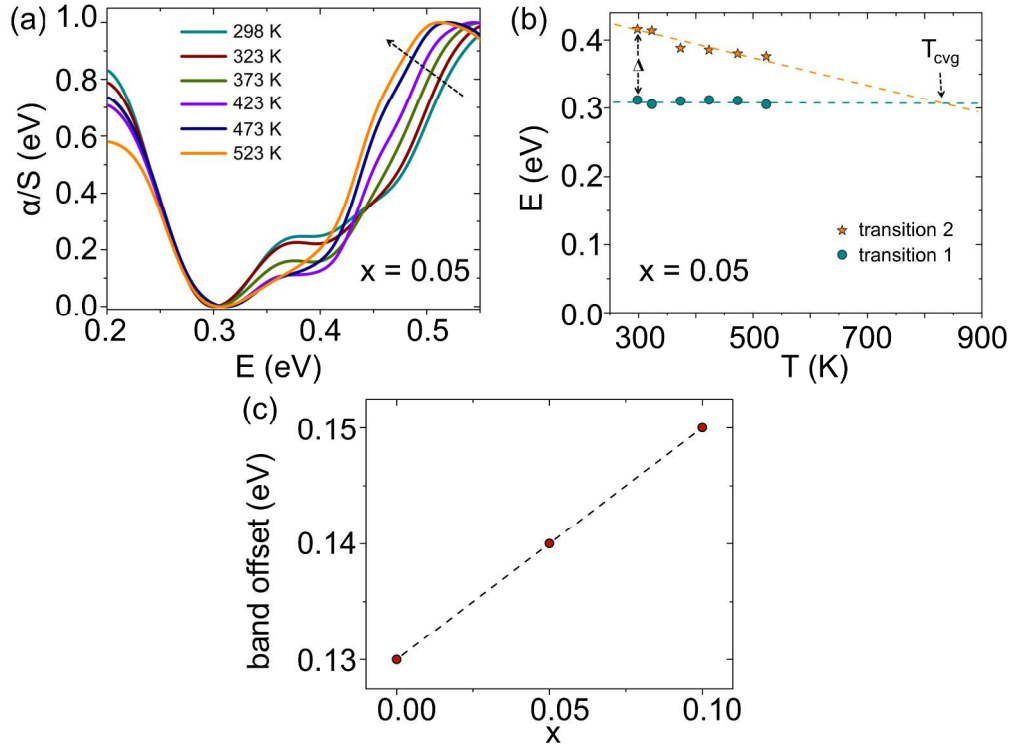

a) optical absorption spectra of BaBiTe2.95Se0.05 as a function of temperature b) changes in energy of transition 1 and 2 as a function of temperature; CB1 and bands higher in the conduction band are converging with temperature; c) band offset as a function of Se content. This image shows that there is band convergence in BaBiTe2.95Se0.05 and that the band offset increases with the Se content.

254x190mm (300 x 300 DPI)

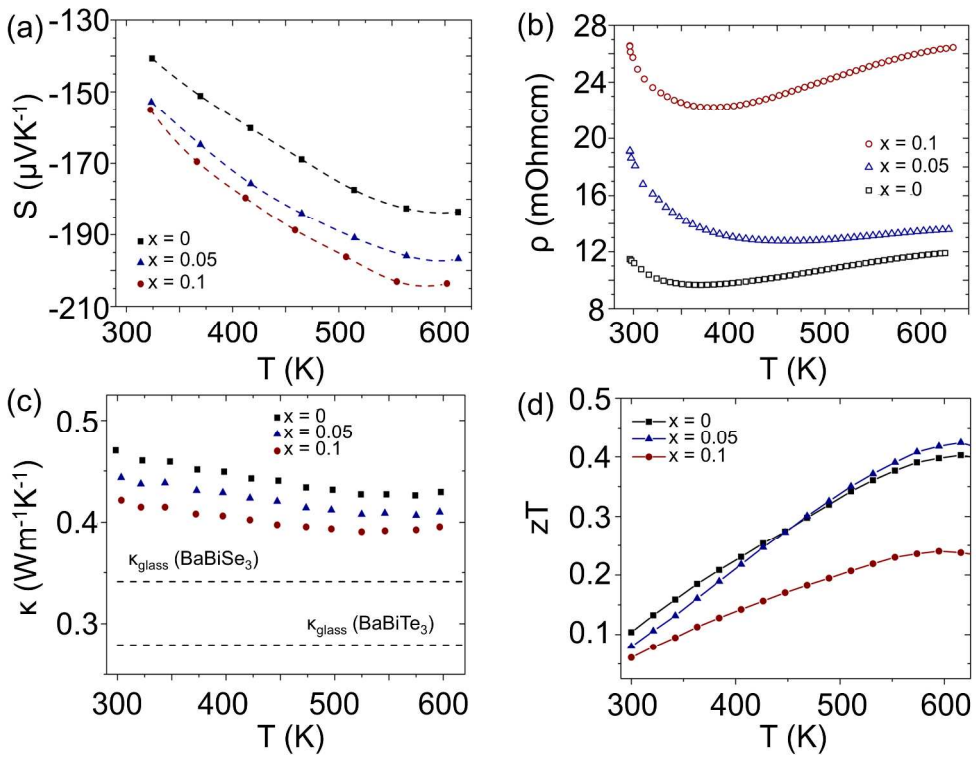

Thermoelectric properties of BaBiTe3-xSex (x = 0, 0.05, 0.1): a) Seebeck coefficient (the dotted lines represent interpolated data), b) electrical resistivity, c) thermal conductivity and minimum thermal conductivity of BaBiTe3 and BaBiSe3 according to Cahill and d) thermoelectric figure of merit (zT).

254x190mm (300 x 300 DPI)

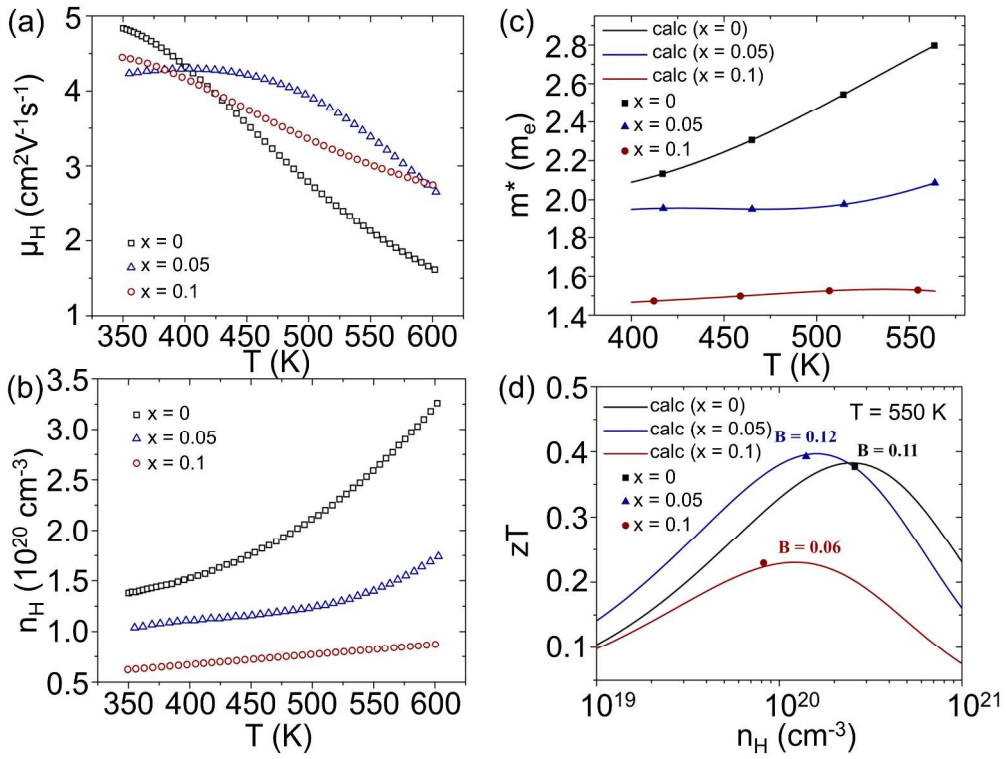

a) Hall mobility and b) hall charge carrier concentration of BaBiTe3-xSex (x = 0, 0.05, 0.1) as a function of temperature; c) calculated zT as a function of hall carrier concentration: lines and symbols correspond to effective band models and experimental data points, respectively; d) "Seebeck effective mass" (m*) as a function of temperature (line and symbols represent calculated m* obtained from interpolated and experimental Seebeck data, respectively). b)-d) show the contribution of CB2 for BaBiTe3-xSex (x = 0, 0.05) in form of an increase in carrier concentration and m* with temperature.

254x190mm (300 x 300 DPI)

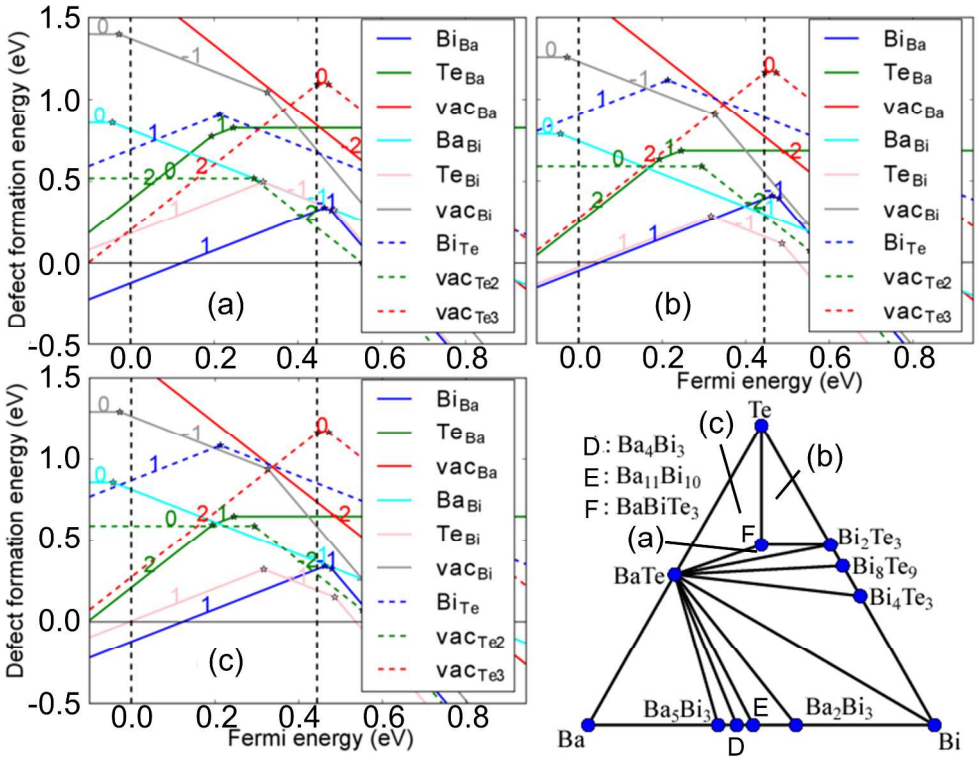

Formation energies of intrinsic defects in BaBiTe3 calculated in three different regions of the Ba-Bi-Te phase diagram: a) region 1: BaTe-Bi2Te3-BaBiTe3, b) region 2: BaTe-Te-BaBiTe3 and c) region 3: Bi2Te3-Te-BaBiTe3; the numbers in each graph correspond to the charge q of the each type of defect. These calculations reveal native BiBa+1 defects with negative defect formation energies close to the valence band edge in all three regions of the phase diagram. These defects are competing with native TeBi+1 defects in the region 2 (b) of the phase diagram for energies close to the valence band edge; these calculations were performed using DFT-PBE.

254x190mm (300 x 300 DPI)